Experimental Mechanics
https://doi.org/10.1007/s11340-022-00925-8

RESEARCH PAPER

An Image Processing Technique to Identify Crack Tip Position and Automate Fracture Parameter Extraction Using DIC: Application to Dynamic Fracture

A. Taylor Owens[1] · **H. V. Tippur**[1]

Received: 11 July 2022 / Accepted: 30 October 2022

Abstract

Background A challenge for experimental fracture mechanics studies using vision-based methods is the accuracy with which the crack tip can be located in the region of interest for extracting fracture parameters. When using full-field displacement measurement methods such as digital image correlation (DIC), positioning the crack tip coordinate system could greatly influence the accuracy of stress intensity factors for brittle materials.

Objective The objective of the present work is to develop improved methods of tracking crack tip position for fracture parameter extraction for problems involving moving fracture fronts (e.g. dynamic crack growth).

Methods An improved image processing-based automated method for identifying the location of a propagating crack tip is proposed here. The primary inputs to the method are two-dimensional displacement fields measured using DIC. An edge detection methodology using a series of partial derivative computations is used to locate the crack tip.

Results The proposed method's performance is verified using simulated displacement fields with a sequence of controlled crack tip positions for mode I and mixed-mode examples. The method is used to locate crack tip positions from mixed-mode dynamic fracture experiments and extract instantaneous stress intensity factor histories. Consistency is shown between baseline and automated methods and post-initiation stress intensity factor histories varied by approximately 5% with the maximum variation being under 10% for the mixed-mode experiments.

Conclusions The automated fracture parameter extraction method produced consistent results with those extracted using traditionally accepted methods, indicating that the proposed automated approach is a marked improvement due to its systematic nature and processing efficiency.

Keywords Mixed-mode fracture · Stress intensity factors · Epoxy adhesives · Automated technique · Digital image correlation

Introduction

Many engineering materials exhibit brittle behavior and fail at low strains. Understanding the failure mechanisms in such materials is of paramount importance for reliable assessment of structural performance. Over the past few decades, several full-field, non-contact, displacement measurement techniques have been proposed for failure characterization. Vision-based full-field methods such as digital image correlation (DIC) have become especially popular in recent years due to simple surface preparation and illumination requirements. While a wide range of experimental methods have been developed over the years for the study of crack propagation behavior, one persistent challenge for these techniques in general and vision-based methods in particular is identification of the crack tip for engineering parameter extraction. Evaluation of stress intensity factors, the J-integral, and other fracture mechanics parameters requires a reliable determination of the position of the crack tip and the direction in which the crack is propagating at that time instant or load-step. For stationary cracks, the position of the crack tip can usually be ascertained more easily using higher magnification of recorded images. In dynamic fracture problems, however, once the crack begins to propagate,

✉ A. Taylor Owens
owensat@auburn.edu

[1] Department of Mechanical Engineering, Auburn University, Auburn, AL 36830, USA

Published online: 13 December 2022

identifying the location of the crack tip is considerably more challenging in general and for materials such as glass and fiber reinforced polymers in particular. Often, the geometry of the crack tip is small relative to the resolution of the measurement technique and surface coatings tend to mask the crack tip. Working with brittle materials that undergo very small deformations at fracture, the displacement field discontinuities at the crack tip are generally not obvious to the operator. The sheer number of temporally distinct images to be analyzed in a dynamic experiment exacerbates the issue as well. Lee et al. [1] noted the challenges associated with crack tip location identification in the study of graphite epoxy composites. Their work estimated an error of at least 0.5 mm in crack tip position due to the relatively small magnitudes of displacements in this stiff, brittle composite. Sundaram and Tippur [2] pointed out the same challenge in their experiments with glass where the choice of the contour increment in the visualization of the displacement field could lead to drastically varying interpretations of the crack tip location. An objective comparison of various optical techniques in [3] revealed the difficulty of crack tip location identification associated with DIC measurements as compared to other methods such as photoelasticity and digital gradient sensing. In general, the post-processing step can quickly become untenable due to the tedious, time-consuming issue of manual tracking of the crack tip that often introduces a significant amount of uncertainty into the results.

Several methods have been used in prior experimental works where there was a need to locate the crack tip position. Fracture parameter extraction from experimental data has been summarized by Redner in [4] and Etheridge and Dally in [5]. The general approach is to utilize a set of analytical equations where stress intensity factors are unknown, and the displacements are known. By choosing a set of points in the field, an over-determined set of equations is formed and can be solved for the unknowns. McNeil et al. [6] utilized such an error minimization technique to extract stress intensity factors from an over-determined set of displacement field equations. The actual crack tip location was taken as the location with the lowest amount of error in the analytical solution. Yoneyama and Takashi [7] proposed an alternative to this where not only the stress intensity factors are unknown, but the crack tip coordinate is also unknown. An iterative procedure was used based on the Newton-Rhapson method where equations were derived to estimate the correction to the stress intensity factor estimation based on the results of the previous guess, such that the procedure eventually converges to a result. This method was numerically similar to that developed by Sanford [8] for extracting stress-optic constants and fringe order from photoelasticity experiments. Pacey and colleagues [9] studied crack closure conditions using photoelasticity. In their work, the analytical stress field was calculated mathematically using Muskhelishvili's stress potential function and the analytical model was fit to the experimental data using a genetic algorithm and the downhill simplex algorithm. Roux and Hill [10] developed a method to estimate the crack tip location using a similar optimization approach by using the digital image correlation data to match the amplitude of a reference displacement field and minimize the error between the measured and reference fields. A method proposed by Hamam et al. [11] utilized the concept of an elastic crack tip and its detection using the first super-singular term in the Williams' expansion. This approach was shown to be relatively robust with an estimated uncertainty of 20 micro-meters in the study of fatigue crack growth in steel. Zanganeh et al. [12] studied several methods based on this concept of minimizing the error between a measured displacement field and an analytical solution. They performed a comparison of multiple Newton-based optimization methods, a direct search method (Nelder-Mead Simplex), a genetic algorithm, and a pattern search method. Their investigation had the best success with the pattern search method which was reported to locate the crack tip within an average of 0.22 mm and 0.04 mm in the x- and y-directions, respectively. More recently, Rethore [13] introduced a method based on elastic regularization along with finite element kinematics on an adapted mesh and a truncated Williams' expansion to identify the crack path. This method was shown to be helpful in the analysis of experiments where the crack is propagating along a curved path.

While the methods discussed thus far are largely focused on optimization-based techniques to fit full field experimental data to an analytical stress or displacement field, the present work seeks to use an image processing-based edge detection technique as the basis for developing a method to improve the accuracy with which the crack tip can be identified. Several methods have been employed to detect crack paths using such image-based techniques. Work by Abdel-Qader et al. [14] explored edge-detection methods to identify cracks present in concrete structures. The work demonstrated the ability to use changes in intensity across an image to locate cracks and crack-like features from images. Lopez-Crespo et al. [15] utilized Sobel edge detection to locate the crack tip to extract mixed-mode stress intensity factors from a tension-shear test geometry. They evaluated the stress intensity factor uncertainty due to position errors and showed relatively low error in the measurement using the Sobel-based technique for fatigue cracks. Separately, a similar approach was used to study cracks propagating away from a fastener hole in [16]. More recently, several authors have made advances in the crack tip location identification problem. Building on recent progress in the field of machine learning, finite element simulations of displacement fields around cracks were used to train convolutional

neural networks [17] and track crack tip position. The method was utilized to study fatigue crack growth in planar 2024 aluminum alloy specimens with a central crack subjected to uniform tension. Miao et al. [18] used Canny edge detection with manual thresholding to approximate the crack path and use the results as a basis for an improved subset-splitting technique. The technique was demonstrated to enable improved reconstruction of the displacement fields near the discontinuity.

In this context, an automated technique based on the Canny edge detection algorithm is proposed here for crack tip identification and subsequent stress intensity factor extraction from measured displacement data. The method is used to locate crack tip position such that stress intensity factors can then be extracted using a hybrid DIC-FE analysis. The proposed method is critically examined using a series of numerical tests from analytical simulations and results are presented from a series of dynamic fracture experiments, demonstrating the ability of the method to allow systematic, controlled extraction of fracture parameters.

Experimental Methods

Displacement Measurement Using Two-dimensional Digital Image Correlation

Two-dimensional digital image correlation (DIC) is a vision-based technique for measuring full-field planar displacements/deformations of an object experiencing load. The method was introduced in the early 1980's [19–22] and has attained maturity and popularity in recent years. The general principle involves applying a random pattern to the surface of an object of interest. As mechanical loads are imposed on the object, the random pattern/speckles follow the deformation of the surface of the object being tested. A digital camera is used to capture a series of speckle images as the object undergoes deformation during a loading event. Once the images are recorded, displacement fields can be computed by comparing subsequent images in the series with the reference image. Image processing techniques are subsequently used to track the surface motion and local deformation. The method and its applications are well documented in [23].

Crack Tip Location

The Canny edge detection algorithm [24] and [25] has been widely demonstrated with good success across a range of image processing problems. The algorithm is typically implemented with the following general steps: Image filtering, gradient calculation, non-maximum suppression, and thresholding.

The first step in the algorithm involves filtering the image to remove noise in the image to aid in the subsequent processing steps. While the smoothing process introduces blur into the image, it reduces the number of edges that will occur simply due to noise in the image. The typical implementation utilizes a Gaussian smoothing function,

$$G(x,y) = \frac{e^{\frac{-(x^2+y^2)}{2\sigma^2}}}{2\pi\sigma^2} \tag{1}$$

where σ is the parameter that determines how much smoothing is applied. In practice, it is convenient to numerically approximate a value for the smoothing function. The matrix defined in equation (2), which is an integer approximation of the case where $\sigma = 1$, provides an adequate level of smoothing for the present work for a 5×5 filtering kernel and can efficiently be applied through a convolution operation.

$$G(x,y) = \begin{bmatrix} 2 & 4 & 5 & 4 & 2 \\ 4 & 9 & 12 & 9 & 4 \\ 5 & 12 & 15 & 12 & 5 \\ 4 & 9 & 12 & 9 & 4 \\ 2 & 4 & 5 & 4 & 2 \end{bmatrix} \left(\frac{1}{159}\right) \tag{2}$$

Once the smoothing has been applied to the intensity values (or displacement field magnitudes in the present work), the gradients within the field can be computed. The underlying assumption with this step is that the edges occur due to sudden changes in intensity in the image and that areas away from the edges are more uniform. One way to measure the magnitude of the change is to calculate the partial derivatives or the gradient magnitudes at each output point. For an image with an intensity I that varies spatially, the first order partial derivatives, $E_x \approx \frac{\partial I}{\partial x}$ and $E_y \approx \frac{\partial I}{\partial y}$, can be approximated for the x- and y-direction. For the typical implementation of the Canny algorithm, the Sobel operator, which is based on two 3×3 filtering kernels, is used to approximate these first order derivatives. This is readily implemented numerically by convolving the filtered intensity field with the kernels:

$$K_x = \begin{bmatrix} -1 & 0 & 1 \\ -2 & 0 & 2 \\ -1 & 0 & 1 \end{bmatrix}, \tag{3}$$

$$K_y = \begin{bmatrix} 1 & 2 & 1 \\ 0 & 0 & 0 \\ -1 & -2 & -1 \end{bmatrix}. \tag{4}$$

This gradient computation was suggested by Sobel and Feldman [26] as an isotropic gradient operator and is widely used in edge detection problems. In practice, this produces a

rudimentary approximation of the partial derivatives, however, it is very efficient from a computational standpoint. The partial derivative magnitude is calculated from the individual directional partial derivative values using:

$$\|E(i,j)\| = \sqrt{E_x[i,j]^2 + E_y[i,j]^2} \tag{5}$$

Once the magnitude and individual partial derivatives in each direction are known, the directions of the gradient vector can be computed using:

$$\theta(i,j) = \tan^{-1}\frac{E_y[i,j]}{E_x[i,j]} \tag{6}$$

These values can be used to further isolates the true edge locations by separating out the possible edge points and guaranteeing that each candidate edge, in the case of the displacement field in DIC, is only one subset point (or one facet) wide. This procedure is known as Non-Maximum Suppression (NMS). An example of implementing this part of the procedure is outlined in Appendix A.

The last step in the Canny edge detection algorithm is thresholding. In the traditional implementation, the points above a certain threshold are identified as edge points and the points below a separate, lower threshold value are excluded from the edge point group. The points in between the threshold values are identified as candidate edge points and are tested to determine if they are connected to points of an edge that were above the higher threshold value. If they are connected to the points that have magnitudes above the threshold, they are included in the group of points belonging to the edge. These threshold values are determined through trial and error and tend to be problem specific. More recently, it has been suggested [27] that an adaptive thresholding method may be more advantageous. In images where there may be a wide range of edge features, one set of upper and lower threshold values might be inadequate to properly categorize the gradient values across the entire image. With adaptive thresholding, not only are the gradient values considered but the overall distribution of gradient values is binned in a histogram. This can be done locally for each subset point in the field of values to adjust the threshold values depending on the local characteristics of the gradient results.

Proposed Method for Identifying Crack Tip

As previously stated, the crack tip identification problem carries many similarities to the edge detection problems in image processing. The general concept is that regions within the displacement field with steep discontinuities must be identified as potential crack faces and within those potential crack faces, the most likely termination point must be identified. In the most basic implementation, the Canny edge detection method described in the previous section can be implemented directly. However, several modifications to the algorithm are necessary to improve its performance to meet the goals of the present problem to include adaptations to the thresholding procedure and specific displacement field preprocessing steps. For the crack tip identification problem, the following methodology is proposed and will be detailed in the following sections. The image space is first decomposed into two domains, one on each side of crack path. DIC is performed on each domain separately, and a Gaussian smoothing operation is implemented on the resulting displacement fields. The partial derivatives and their magnitudes and directions at each output point are calculated, and an algorithm (described in the previous section) is used to suppress non-maximum values. A histogram of the gradient values is calculated and used to determine the far-field component of gradient to remove spurious edges. The general workflow of this process is outlined in Fig. 1.

Displacement Field Decomposition

The first step in the proposed procedure is to identify the edge of the fractured specimen (or the crack path) and use it to split the image space into two separate domains. The path is identified by first selecting an image that contains the fully propagated crack. The image is manually marked with a series of points along one of the two crack faces and then imported into MATLAB®. Once in MATLAB®, the points along the manually marked edge are located using an image of the specimen after full separation. The rigid body motion is calculated using two images, one from prior to loading state and the second after separation/fracture. Multiple points along the specimen edge or crack face are extracted from an image captured prior to loading and compared with the same edge points extracted from an image captured after full separation. It is assumed that the specimen deformation is dominated by recoverable elastic deformation. The calculated rigid body motion (displacement and rotation) is used to transform the crack edge from the deformed coordinate system back into the undeformed coordinate system to remove the rigid body motion. The edge in the undeformed coordinate system is then used to create

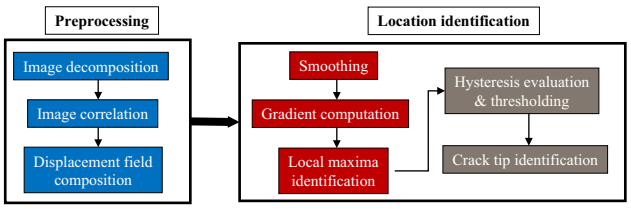

Fig. 1 Workflow for the proposed crack tip detection/location procedure

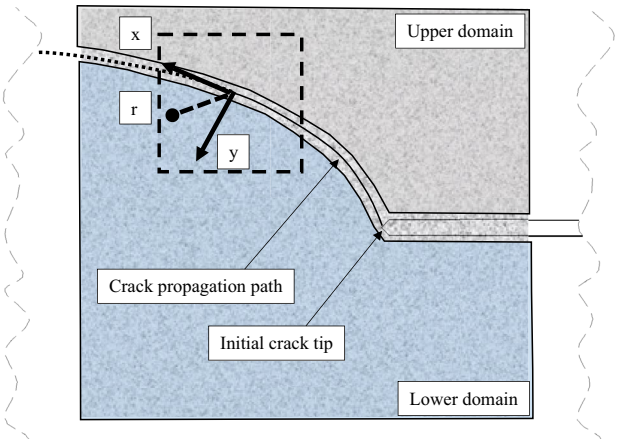

Fig. 2 Upper and lower image correlation domains as they relate to the position of the crack tip and crack propagation path

the boundary between the upper domain and the lower domain for the image correlation procedure as illustrated in Fig. 2. This results in an upper domain mask (all pixels outside of the upper domain are removed from the image correlation procedure) and a lower domain mask (all pixels outside the lower domain are removed from the image correlation procedure).

By splitting the image into two separate domains, one on each side of the fracture surface, the image correlation process can utilize subset truncation which allows correlation to be performed on partial subsets as illustrated in Fig. 3. For points within the image that are close to the edge, truncating subsets enables displacement data to be acquired within a few pixels of the edge. As the crack propagates across the specimen, each individual domain remains continuous, and subsets are not allowed to cross the boundary between the two domains. In those situations, pixels from both domains are considered in the correlation and either correlation quality degrades, or the displacement becomes smeared or averaged across the boundary/edge (or the crack in the present case). The truncation avoids these two forms of data degradation.

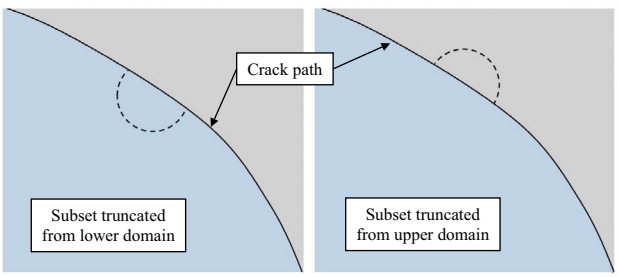

Fig. 3 Subset truncation illustration showing lower domain subset truncated at boundary (left) and upper domain subset truncated at boundary (right)

After the images are processed, the two domains of displacement data are stitched back together. Since the masks for the decomposed domains were created in the same original image space and the same images are used for the correlation process, the resulting two displacement field sets also exist in the same image reference space. That is to say that each data array has numeric values for each subset within its own domain and is zero padded in areas outside of its domain. These data arrays can thus be stitched together via a simple matrix addition operation. The two displacement fields are imported as 2-dimensional data arrays into MATLAB® and added together resulting in a single 2-dimensional array consisting of a continuous field of data ahead of the crack tip and a discontinuous field of data behind the crack tip for any given point in the crack tip propagation history. It should be noted that a minimal amount of noise is present ahead of the crack tip that will be addressed in later sections.

Displacement Field Gradient Estimation

The resulting displacement field is then normalized to create a normalized displacement field, $I(x, y)$, associated with each component of displacement such that the maximum value is 1 and the minimum value is 0. This is calculated as,

$$I(x,y) = \frac{\delta(x,y) - \min\{\delta(x,y)\}}{\max\{\delta(x,y)\} - \min\{\delta(x,y)\}} \tag{7}$$

where δ can be the taken as the global x-direction displacement (u), the global y-direction displacement (v), or the magnitude of the displacement ($\sqrt{u^2 + v^2}$). The displacement components can be given equal weight in subsequent analysis steps or could potentially be weighted towards the more dominant displacement component.

The normalized displacement field is then convolved with the Gaussian filtering kernel defined in equations (1) and (2), resulting in a smoothed version of the normalized displacement field. The intensity gradients are then computed from the filtered intensity field using 2-dimensional convolution of the filtered intensity values with the kernels, K_x and K_y, to calculate the desired partial derivatives in the x- and y-directions, respectively.

Crack Edge Estimation

The magnitude of the partial derivative results and the directions are computed using equations (5) and (6), respectively. The non-maximum suppression (NMS) technique is then used to thin the edge down to obtain an edge that is a single data point wide. In the present work, an additional step is taken at this point to filter out points that are known to lie away from the actual crack path. Since the edge is known

and the crack tip must lie on that edge, the points away from the edge can be removed from the group of candidate points (for instance the specimen edges). This step is handled automatically by calculating the Euclidean distance of each candidate point to the known crack path.

Thresholding

The final step is to identify the most likely position of the crack tip within this subset of candidate points of the edge. The typical method in image processing problems is to use an approach referred to as adaptive thresholding, similar to what has been proposed by Rong et al. [27]. This approach takes a histogram of the field of partial derivative values and selects a threshold value that results in a certain percentage of output data points occurring above the threshold and a certain percentage of points falling below the threshold. This has been shown to work well on certain image processing problems, however, it is still subjective, and does not appear to be sufficiently robust for the crack tip identification problem at hand, and thus, a more robust approach is desirable. For the present implementation, a histogram of the partial derivative is first taken, and used to compute the distribution of the partial derivative values. An example histogram is shown in Fig. 4 from a mixed-mode crack problem to be discussed later.

One interesting feature of the histogram is that it has a distinctive peak at a magnitude of 0 and a secondary distinctive peak at another non-zero value. The first peak occurs near 0 and accounts for the majority of the data in the partial derivative field where the strain in the material is relatively low (as compared to the discontinuous crack faces). This has been truncated in the figure to see the secondary peak more clearly. This secondary peak is attributed to noise in the partial derivative field ahead of the crack tip and also away from the gradients associated with the crack faces which are much higher in magnitude. The second peak, centered at a magnitude of approx. 0.04 for the example, is relatively subtle, but can be used for filtering out additional unwanted edge candidates. For the present implementation, this secondary peak was used to separate spurious far-field data from the location of the crack tip. There is relatively high confidence that partial derivative values that are higher than this secondary peak occur on the crack faces behind the crack tip. A series of values were selected that were known to be slightly higher than this secondary peak and used for tracking the crack tip position. The thresholding procedure is adaptive in the sense that the value of the far field noise can fluctuate as the displacements evolve and can ensure that the points that are being tracked are above this noise threshold. The crack tip is then taken as where the partial derivative values regress towards a value slightly higher than this secondary value that is above the far-field noise. Since there is still uncertainty as to whether the crack tip is precisely located at this location, the positional error can be estimated based on the initial data sets where the crack tip is stationary and the physical crack tip is known. Locations of the propagating crack tip can be corrected for this error since it is known with relatively good confidence.

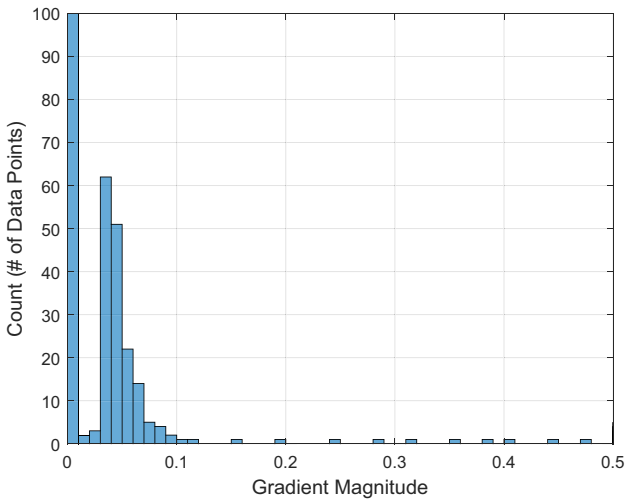

Fig. 4 Example histogram of gradient data showing pronounced secondary peak due to noise in the gradient field ahead of the crack tip

Stress Intensity Factor Extraction

Once the crack tip positions for the propagating crack are known, the stress intensity factors can be extracted. Two methods are utilized in the present work for evaluating stress intensity factors. The first method utilizes the measured displacements to estimate the stress intensity factors by fitting a set of over-determined equations to the displacement field around the crack tip. This procedure has been widely used in the fracture mechanics community. The details are given in Appendix B for completeness. The second method utilizes a domain integral approach to extract the stress intensity factors as described in the following section.

Domain Integral Approach

The stress intensity factors can also be extracted using a domain integral approach. The J-integral, as presented in Shih et al. [28], is defined as:

$$J = \int_A \left(-W\,\delta_{ij} + \sigma_{ij}\frac{\partial u_j}{\partial x_1} \right) \frac{\partial q_1}{\partial x_1} dA,\ (i,j = 1,2) \tag{8}$$

where A is the area of the domain or the area that includes the crack tip being evaluated, q_1 is a weighting function that equals 1 on the outer boundary of the domain and 0 on the

inner boundary of the domain. In the case of the plane stress condition, this domain integral can be decomposed into the two stress intensity factors K_I and K_{II} for modes I and II, respectively, using the relationship:

$$J = \frac{1}{E}\left(K_I^2 + K_{II}^2\right) \tag{9}$$

The Abaqus finite element software employs an interaction integral technique to partition J and extract the two stress intensity factors based on the technique described in [29].

To implement this approach, the experimentally measured displacement data is filtered to minimally remove noise and a post-processing script is used to calculate the coordinates of each of the subset points based on the known pixel size, subset size, and subset spacing. The grid of DIC output points is structured with uniform spacing in the x- and y-directions. Once the nodal coordinates are known, the script utilizes the array indices of the nodal position data to establish the element connectivity using the Abaqus element connectivity convention where the first node is in the lower right quadrant. Other nodes of the element are ordered in a counterclockwise direction. Once the nodal positions and element connectivity have been determined, the script then writes the node and element data into a text file in the proper Abaqus input file format. Lastly, the script writes the material property definitions for the model, and the appropriate output requests to extract the fracture parameters of interest using the previously described domain integral approach using the Abaqus structural solver. This approach has been documented by the present authors in [30] in the study of rubber-toughened epoxy specimens with inclined cracks as well as in [31] in the study of the effects of print architecture on fracture of additively printed ABS. Both aforementioned works have critically examined this approach and for brevity the details are avoided here.

Verification

Two separate finite element models were utilized to study the performance of the proposed edge detection algorithm for the crack tip problem and establish confidence in its performance. The intent of the verification was to ensure that the methodology correctly meets the objectives of positively identifying the crack tip where the crack tip is known a priori. Verifying the performance of the methodology provides an opportunity to investigate the confidence with which the crack tip can be located. Additionally, it establishes the sensitivity to certain parameters and assumptions inherent to the procedure, namely the resolution of the experimental displacement data. The verification procedure also enables the investigation of the ability of the algorithm to perform on more challenging fracture problems such as those involving higher elastic modulus materials of low fracture toughness where experimentally measured displacements are substantially lower in magnitude at failure.

The proposed verification process for the automated method is to create a set of displacement fields using numerically-simulated crack problems to test the methodology. The algorithm implemented in the present work is primarily developed and scripted to work with data structures analogous to those found in image processing problems. More specifically, for the present problem, displacement data at uniformly spaced points in an orthogonal coordinate system. Thus, the numerically-simulated data was mapped onto such a uniform grid of points.

Mode I Verification

A simple three-point bending model with an edge crack, loaded in mode I was used for the first test. This is a relatively straightforward model for test purposes due to the known self-similar crack path, and the fact that one of the displacement field components accounts for a majority of the crack face motion. The beam had a height of 38 mm, length of 203 mm, and support span of 152 mm. The length of the edge crack was varied from 12.7 mm to 25.4 mm in 2.5 mm increments. The boundary conditions and displacement field from the finite element model are illustrated in Fig. 5. The first case used an elastic modulus of 2.2 GPa, similar to the modulus of the material in the present work and the applied load in the model was scaled to a target stress intensity factor of 1.1 MPa-$\sqrt{\text{m}}$.

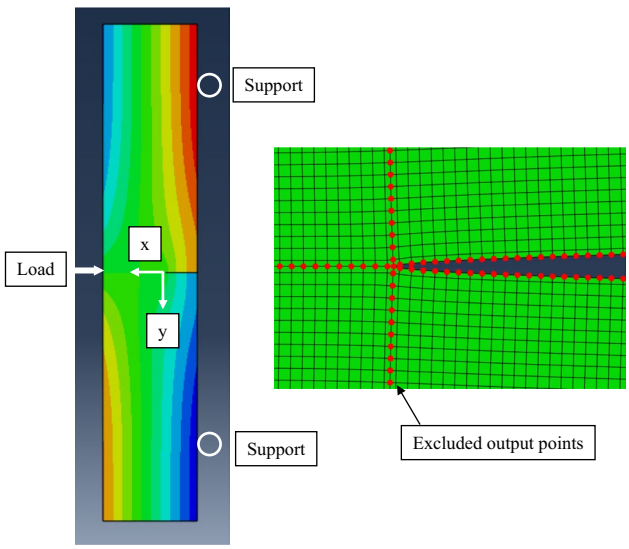

Fig. 5 Finite element model and crack tip mesh detail used for edge detection verification

For this first test problem, the mesh around the crack tip was structured to artificially mimic the positioning of the output points from the experimentally measured digital image correlation data such that the methodology could be tested directly using the nodal output calculations. As shown in the figure, the nodal output points along the crack faces and directly ahead of the crack tip (highlighted in red) are ignored in the edge detection algorithm since those points would not physically be reported in the digital image correlation output data. The remaining output points are uniformly spaced as would be the case for a typical output set from digital image correlation.

Crack Tip Location Comparisons

For each analysis run, the crack edge was manually extended, thus repositioning the crack tip to a new, known position. The displacement field from the finite element model was then extracted using a python script and subsequently read into MATLAB® into the same data format as the typical digital image correlation results.

For the purposes of gaining insight into this method, for this simple initial test case, the maximum gradient value was extracted at each horizontal position in the displacement field (e.g., specific distance from the edge). As expected, behind the crack tip, the gradient approaches some constant value. These values are plotted for each successive crack tip position in Fig. 6. The contour plot is uniform away from the crack primarily because the magnitudes of the gradient values away from the crack fall into a very small range compared to the large gradients present across the crack faces.

The colored vertical dashed lines in Fig. 6 are plotted for reference to show the horizontal position of the actual crack tip. The black horizontal dashed line is approximately aligned to the point on the gradient plot where the actual crack tip resides. As shown in the figure, it is evident that the crack tip position occurs generally in the same location relative to the far field gradient ahead of the crack tip. For this simple test case, it was relatively straightforward to manually identify an appropriate threshold value and track that value as the crack tip propagates in space thus using the simplest implementation of the Canny edge detector. For this test problem, the estimated crack lengths from the edge detector are tabulated in Table 1. The estimated values agree well with the actual crack tip positions with the amount of error decreasing with crack length, implying that the error is a constant value irrespective of crack length.

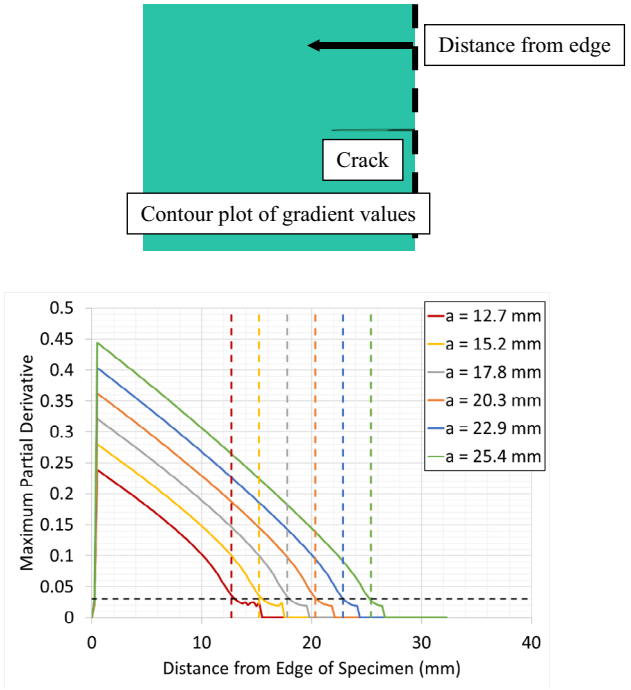

Fig. 6 Contour plot of gradient (equation (5)) values (upper) and line plots of maximum intensity gradient values (lower) at different crack lengths

Mixed-mode Fracture Verification

The three-point bending geometry demonstrates the feasibility of the general procedure and workflow of the edge detection algorithm. However, the mode I behavior produces a relatively simple displacement field around the crack tip, namely, the dominant direction of the displacement field is well understood. Additionally, the algorithm performs well even by simply thresholding the gradient results (partial derivatives of displacement in each direction) manually. To demonstrate the full utility of the methodology, it is necessary to investigate its use on more complex geometries and more complex displacement fields. For this next level of verification, a semi-circular beam geometry was selected. First, this geometry can be configured for a full range of mode mixities [30],

Table 1 Edge detection algorithm accuracy study on simple mode I crack problem

Position	Actual Crack Length (mm)	Estimated Crack Length (mm)	Difference
1	12.70	13.24	4.3%
2	15.20	15.73	3.5%
3	17.80	18.20	2.2%
4	20.30	20.64	1.7%
5	22.90	23.05	0.7%
6	25.40	25.45	0.2%

and second, the geometry creates a crack propagation path that is not self-similar. This part of the verification was divided into two key sections. First, a finite element model was setup to provide simulated displacement fields. From a failed specimen from a mixed-mode fracture test, a representative crack path was extracted so that different crack tip locations along that crack path can be simulated using the numerical model. Second, an inverse finite element mapping tool was developed and utilized to transform the simulated displacement fields into an array of vertical displacements and an array of horizontal displacements, both output onto an uniformly spaced grid of output points. This mapper was necessary because the geometry of the propagating crack path does not lend itself to creating a structured mesh as in the mode-I case (details follow).

Test Specimen Geometry

The semi-circular beam (SCB) test specimen geometry was first introduced to study mechanics problems involving cored concrete and rock [32–34] cylinders. The general specimen geometry and loading configuration are illustrated in Fig. 7 where R is the radius of the specimen, a is the crack length, β is the crack angle with respect to the horizontal axis of the specimen, and S is the half span. The Cartesian crack tip coordinates are denoted by the x- and y-axes parallel and perpendicular to the crack, respectively. The corresponding crack tip polar coordinates r and θ are as shown.

As investigated in [34], the stress intensity factors at the crack tip, and therefore the mode mixity, are controlled by the geometric parameters of the test setup namely, R, a, β, and S. For the purposes of this study, a single initial crack orientation was selected with several subsequent analyses of crack tip points located along a projected hypothetical crack path.

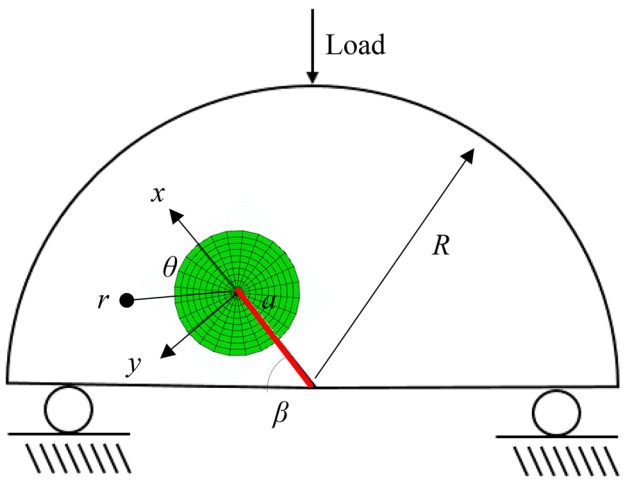

Fig. 7 Semi-circular beam bending test configuration for quasi-static case, shown with typical crack tip mesh

SCB Finite Element Model

The specimen section of the finite element model is shown in Fig. 8. The coordinates for the crack path from a failed test specimen were extracted and imported into the finite element software to partition the domains along the physical path. A series of analyses were then performed by manually advancing the crack tip incrementally along the path. This provided a series of displacement field results representing a range of mode mixities and a range of orientations to test out the edge detection algorithm.

The FE model does not create output on a uniformly spaced grid of points; however, the proposed crack tip location identification technique is formulated to operate on uniformly spaced output data. Because of specimen geometries, crack orientations, crack propagation paths, etc., the elements found within the FE mesh for each crack propagation step can have a variety of shapes and thus the nodal displacement data is not able to be output on a uniformly spaced grid. To that end, an inverse FE mapping technique was implemented in MATLAB® to map the output data from the FE model (nodal displacements in the x- and y-directions). This concept has been shown to be a viable method for mapping between two coordinate spaces by several authors including [35] and [36]. The details of the mapping process are documented in Appendix C.

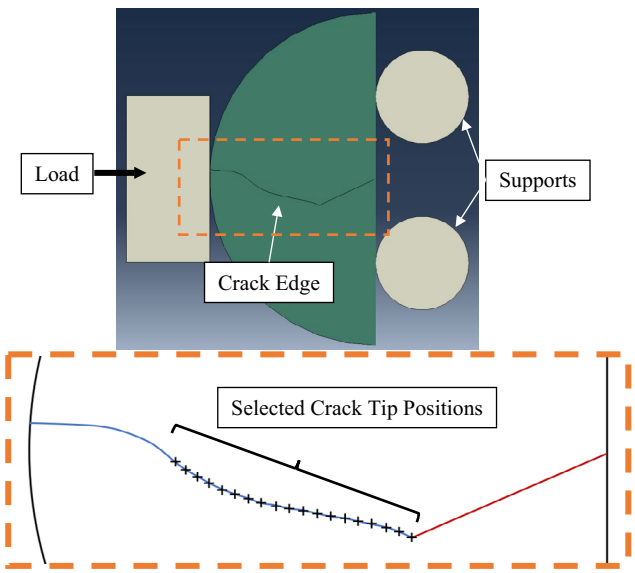

Fig. 8 Specimen section of finite element model

Mapping Checks

The mapping scripts were tested to ensure that the simulated data from the FEA is being properly represented in the evenly spaced grid output data used for testing the robustness of the edge detection algorithm. A comparison is shown in Fig. 9. The two displacement fields match in terms of magnitude and distribution. The crack faces appear to be properly represented in the mapped displacement field.

Prediction Comparisons

The simulated displacement fields from the SCB model were used to further test the edge detection algorithm performance for several specific scenarios to demonstrate its utility. This test case was a mixed-mode fracture case where the crack initiates under shear-dominated conditions and then transitions to tension-dominated growth. This is an excellent verification case because the crack face motion is initially dominated by sliding between the two crack flanks at the initial crack tip location, but as the crack propagates, it transitions to being dominated by opening between the two. The Sobel gradient operator is

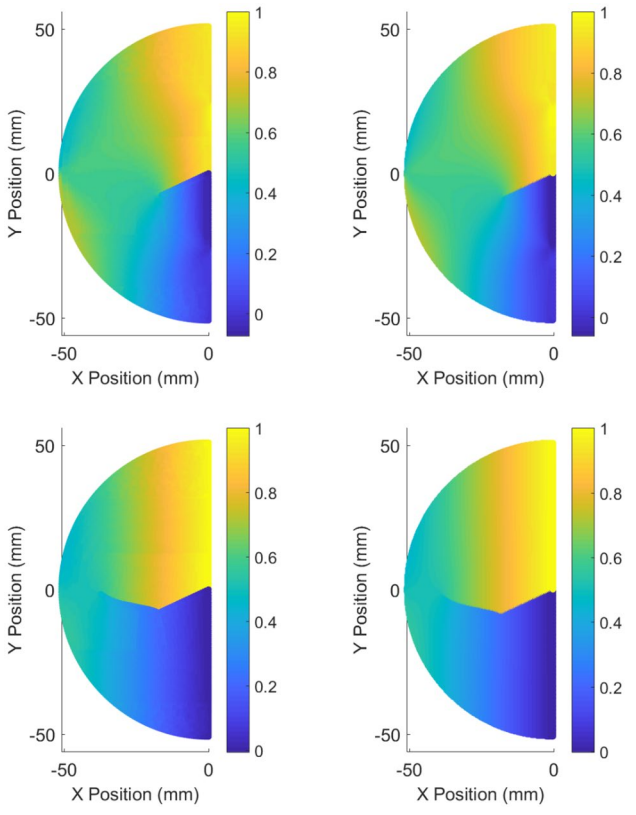

Fig. 9 Source normalized displacements from simulation (left) compared with mapped normalized displacements (right) for two different crack tip positions

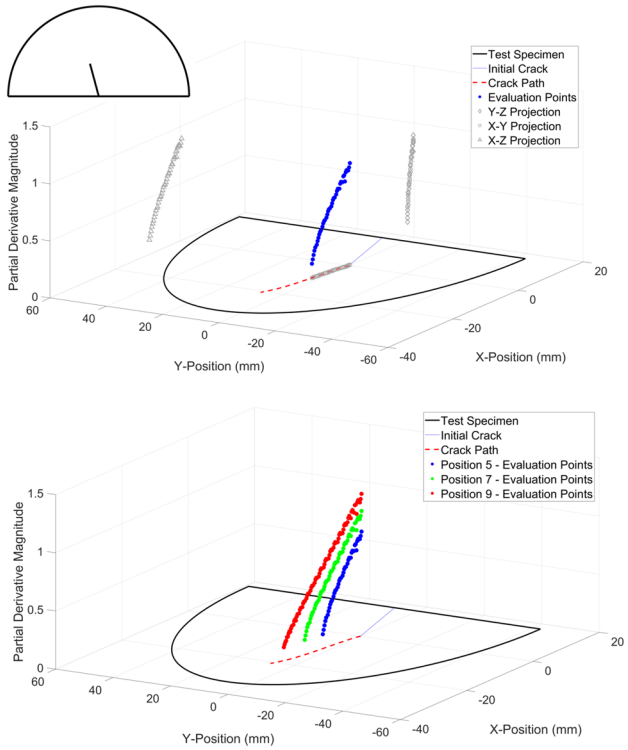

Fig. 10 Field of partial derivative values illustrated in 3D space for single crack tip location originating from an inclined crack (top) and evolution of partial derivative values as crack propagates in the x–y plane (bottom)

generalized to compute partial derivatives in both directions, so this case exercises the full range of possible partial derivatives and directions. This part of the process is illustrated in Fig. 10. The x- and y- positions are the planar coordinates in the displacement field space, and the z-position is the magnitude of the gradient with the origin of the coordinate system located at the original crack tip. A projection of the specimen boundaries is also plotted for reference. This figure shows how the partial derivatives are much higher at the furthest locations from the crack tip location and they progressively approach zero at the crack tip. However, due to noise, the thresholding procedure is used to track a point at a small, but known, distance away from the crack tip. The gradient values are separately plotted in three-dimensional space for a series of crack tip locations to illustrate the evolution of the partial derivative computations as the crack propagates. The simulations were performed with the same material properties as the mode I test case (elastic modulus of 2.2 GPa, with load applied to a target stress intensity factor of 1.1 MPa-$\sqrt{\text{m}}$).

Using the results from this set of simulations, a series of test cases were run to examine the behavior of the algorithm and determine relationships between algorithm parameters

and their ability to locate the crack tip. This work was split into four separate studies: first to study the thresholding value, second to determine the effect of subset/grid spacing, third to determine the effect of the Gaussian blur kernel size, and forth to study the effect of the Gaussian smoothing parameter. The operator has flexibility in choosing these parameters. The study parameters are summarized in Table 2.

The range of threshold values was based on an investigation of the distribution of gradient magnitudes in the image (see Fig. 4 for reference). The range of sub-image/facet spacing values were chosen based on the desired subset spacing for the DIC data extraction. With respect to the Gaussian filter parameters, three plausible values were chosen based on several open source example problems.

The comparison of crack coordinate position is shown in Fig. 11. Figure 11(a) and (b) show the effects of threshold value and subset/grid spacing whereas Fig. 11(c) and (d) show the effects of kernel size and sigma values. (Note that the values are plotted in terms of the static X–Y coordinate system centered at the initial crack tip and as illustrated in the inset in Fig. 11 which is different from the instantaneous crack tip coordinate system (x, y) reported elsewhere).

These plots in the X–Y coordinate system illustrate that generally the prescribed crack path is the shortest distance and the fact that the estimated crack tip points oscillate between one side and the other of the actual path, the edge detection algorithm tends to overpredict total crack length. With regard to investigation of the threshold parameter, a value of 0.1 (accompanied by the subset spacing of 0.25 mm) worked particularly well for this test problem. The most significant effect with respect to thresholding occurred in case #1 where a low threshold value (0.05) was greatly influenced by noise in the gradient estimation near the crack tip and hence had a poor outcome on the crack tip position identification. With respect to the grid spacing, case #5 which had the largest grid spacing (0.5 mm), had a few results with noticeably large position errors approaching 1 mm; however, on average, it performed similar to the other cases analyzed across many of the test points. The effect of Gaussian kernel size was minimal. Almost no difference was found between the 5×5 kernel size and the 7×7 kernel size. With respect to the choice of σ, a value of 1.0 was found to produce acceptable results, with the higher and lower values potentially introducing too little or too much smoothing. In general, the automated procedure was able to locate the crack tip with a high degree of accuracy. For most of the test cases, the average location error across each of the 10 test locations ranged from 0.2 mm to 0.4 mm. Only select cases exceeded this range with case #1 having the highest average error (1.33 mm), followed by case #3 (0.46 mm) and case #9 (0.48 mm). Considering that the algorithm is operating on a grid of uniformly spaced data, the algorithm should be able to detect the crack tip position to within 1 increment of the spacing of the gridded data which seems to be reflected in this study. For the present work, it was determined that the thresholding procedure documented in earlier sections would maintain threshold values that were within a favorable range based on this study. A spacing value of 0.36 mm was chosen. It performed well in the correlation procedure while fitting within the range of values that worked well on the test problem. A Gaussian filter kernel size of 5×5 was chosen and implemented with $\sigma \approx 1$.

Experiments

Next, the Canny edge detection concepts along with numerically driven demonstrations of the algorithm to precisely identify the crack tip via simulations was put to test by performing

Table 2 Edge detection algorithm parameters

Variable	Case Number	Gaussian Filter Kernel Size	Gaussian Filter Sigma Value	Threshold Value	Grid Spacing (mm)
	1	5×5	1.0	0.05	0.250
Threshold	2	5×5	1.0	0.10	0.250
	3	5×5	1.0	0.20	0.250
	4	5×5	1.0	0.10	0.125
Grid Spacing	2	5×5	1.0	0.10	0.250
	5	5×5	1.0	0.10	0.500
	2	5×5	1.0	0.10	0.250
Kernel Size	6	3×3	1.0	0.10	0.250
	7	7×7	1.0	0.10	0.250
	8	5×5	0.5	0.10	0.125
Sigma Value	2	5×5	1.0	0.10	0.250
	9	5×5	2.0	0.10	0.500

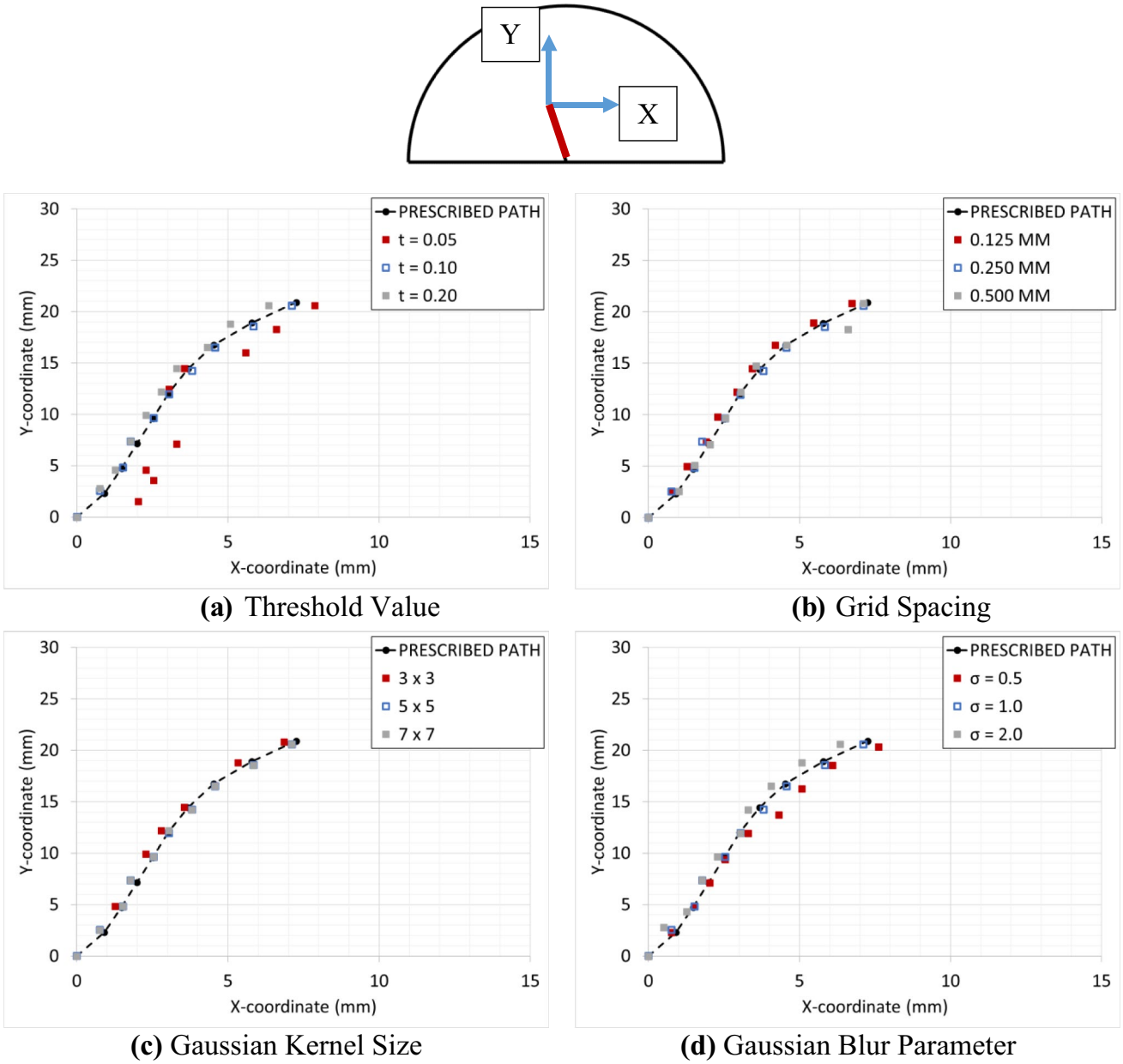

Fig. 11 Effect of edge detection algorithm parameters on crack tip location. (Note that X and Y represent spatial coordinates, different from the crack tip coordinates, x and y)

an actual dynamic fracture experiment. The details are as follows.

Test Setup

In order to evaluate the fracture quantities of interest, a long bar apparatus was utilized for subjecting an SCB test specimen with an inclined crack to a dynamic loading event. The test setup is shown schematically in Fig. 12. In this setup, a gas gun was used to accelerate a 305 mm long, 25.4 mm diameter 7075-T6 aluminum striker bar up to the desired velocity. The striker bar was propelled to impact a 1.83 m long, 25.4 mm diameter 7075-T6 aluminum long bar. The striker bar creates an elastic longitudinal stress wave that propagates the length of the long bar into the test specimen. A strain gage located on the long bar enables measurement of the load history that is being transmitted to the test specimen.

A trigger and a delay generator are used to control the image acquisition through a Kirana-05 M ultrahigh speed camera. The camera is equipped with a 924 × 768 sensor with 10-bit gray scale resolution. A Nikkor 80–400 mm

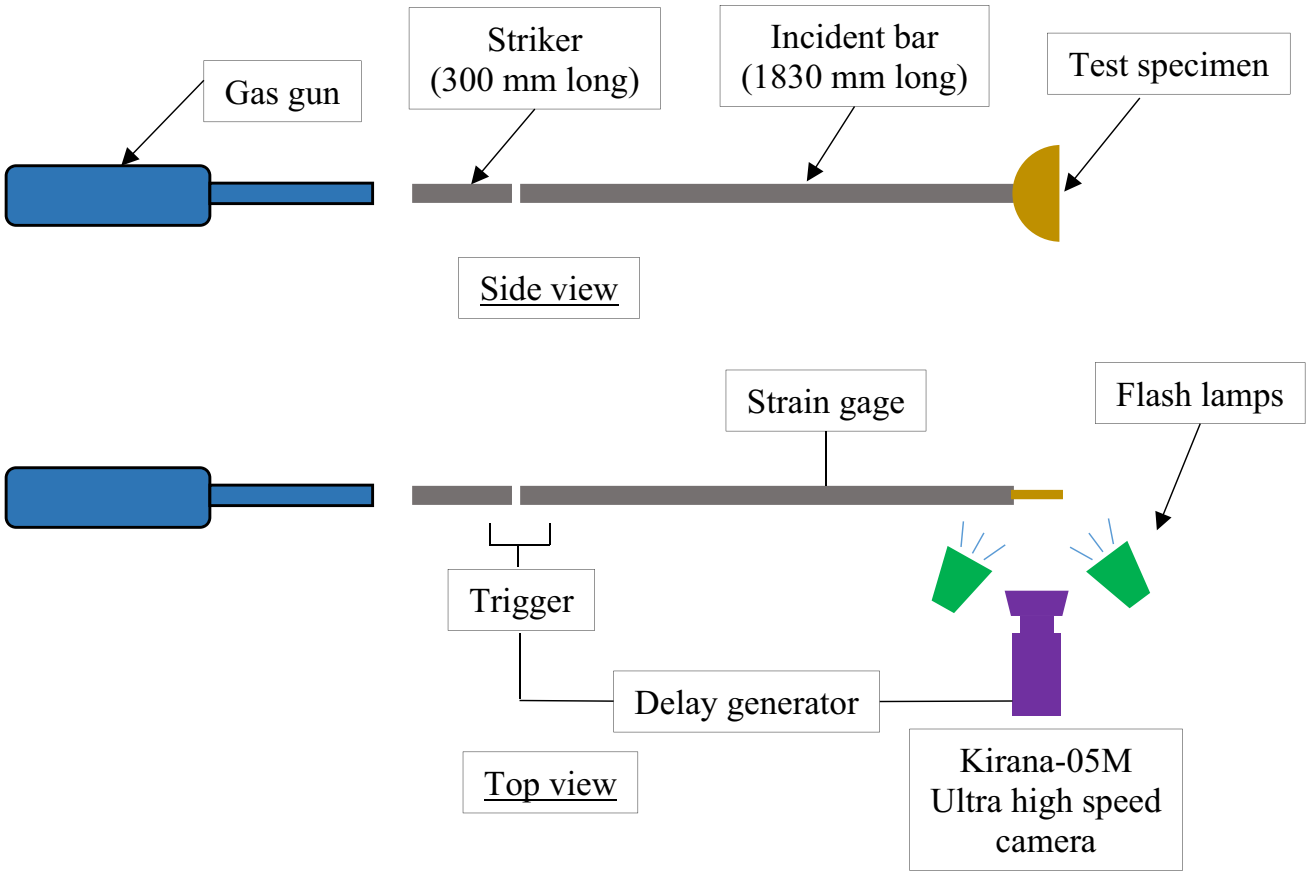

Fig. 12 Experimental setup (side view and top view) of stress wave loading apparatus for dynamic mixed-mode fracture

focal length macro zoom lens with a focal length doubler was utilized. The camera can acquire up to 180 images of the dynamic event at up to 5 million frames per second. A frame rate of 500,000 frames per second was used for the current work. The Ncorr [37] software was used to perform the speckle image correlations to quantify displacements in the two orthogonal in-plane directions. Based on the subset spacing (5 pixels), and the pixel scale factor (~0.06 mm), the resulting distance between neighboring output points was 0.36 mm. The parameters for the digital image correlation setup are summarized in Table 3.

Dynamic fracture specimens were fabricated for demonstrating the proposed experimental procedure. A rubber-toughened epoxy formulation representative of a broad range of epoxy-based adhesive materials was chosen for the present work. It was a basic mix of EPON™ 828 epoxy resin

Table 3 Summary of digital image correlation parameters

Hardware Parameters		**Analysis Parameters**	
Camera Manufacturer	Kirana	Software	NCORR
Camera Model	05 M	Manufacturer	Open source
Image Resolution	924 × 768	Image Filtering	Guided filter
Lens Manufacturer	Nikkor	Sub-image Radius	45 pixel
Focal Length	80–400 mm	Step Size	5 pixels
Field of View	50 mm × 50 mm		
Image Scale	16.7 pixels/mm		
Stereo Angle	N/A		
Image Acquisition Rate	500,000 fps		
Patterning Technique	Ink stamp		
Approximate Feature Size	5–7 pixels		

Table 4 Test specimen material properties

Elastic modulus	2.2 GPa (± 0.2 MPa)
Poisson's ratio	0.33
Density	1107 kg/m^3

and EPIKURE™ 3234 curing agent. Based on manufacturer recommendations, the two components were mixed at a ratio of 100:13 by weight. Prior to mixing, the resin was heated to 66 °C. Core–shell rubber particles were then mixed in at a ratio of 10% by weight using a Flaktek speedmixer. The speedmixer is a dual asymmetric centrifuge planetary mixer that reduces the opportunity for air entrapment in the mixer. After mixing, the mixture was allowed to cool to room temperature prior to adding the amine-based hardener and mixing it further. The epoxy mixture was then poured into the mold cavity. A sharp razor was inserted into the mold with the help of a template to align the razor blade to the desired inclination angle. A clip was attached to the razor blade to hold it in place while the epoxy cured. The samples were cured for approximately 18–24 h at room temperature followed by a post cure step for 2 h at 93 °C. The face of each test sample was then milled flat to the desired nominal thickness of 6.4 mm. Flat white paint was applied to the face of the test sample followed by a random speckle pattern created by a textured ink stamp. The material properties of this epoxy formulation are summarized in Table 4. Further details regarding the static and dynamic characterization of this material are available in [38].

The specimen geometry (illustrated in Fig. 7) is a semicircular beam of 50 mm radius and edge crack of length 19 mm. The specimen is loaded by the long bar as illustrated in Fig. 12. It should be noted that this dynamic load case is a single point, inertially driven loading event different from the 3-point supported quasi-static geometry in Fig. 7. The specimen is lightly held in alignment at the end of the bar with a short strip of soft putty along its edges. The proposed test setup and specimen geometry has separately been critically evaluated in [38]. By changing the crack inclination angle and/or the impact velocity, the specimen mode mixity at crack initiation can be controlled by assuming a known crack initiation toughness. This is illustrated in Fig. 13 where mode mixity is plotted as a function of crack inclination angle for three different striker velocities. The mode mixity is calculated as $\varphi = \tan^{-1}\frac{K_I}{K_{II}}$ at the instant when the stress intensity factor reaches a critical value, $\sqrt{K_I^2 + K_{II}^2} > K_{CR}$.

For the present work, tests were performed with an impact velocity of 8 m/s and crack inclination angles ranging from 90° (pure mode I) to 65° (pure mode II) to test the edge detection against a range of dynamic displacement field histories and resulting mode mixity conditions. Three separate experiments were examined critically to evaluate

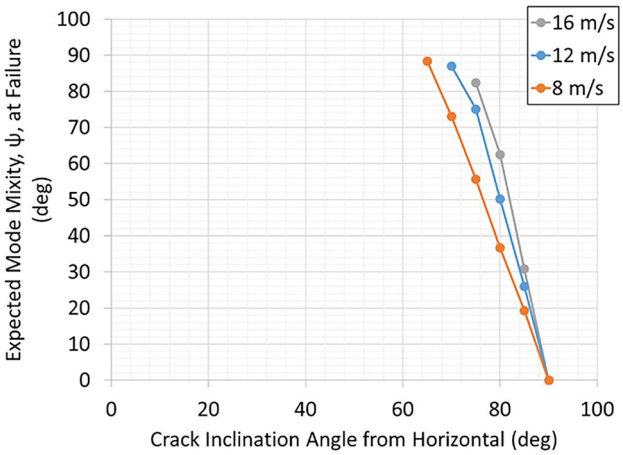

Fig. 13 Mode mixity values for different crack angles for different striker velocities

the performance of the proposed crack tip detection method. The crack tip positions and velocities were extracted using the edge-detection technique detailed earlier followed by the stress intensity factors at different instants of time.

Results and Discussion

Displacement Field Considerations

Displacement contours from one of the mixed-mode experiments (80° from the specimen edge) are plotted in Fig. 14. The contours presented in the left-hand column are taken just prior to crack initiation and the contours presented in the right-hand column are at 30 μs after crack initiation. The top row contains sliding displacements (x-direction displacements in the local crack tip coordinate system) and the lower row contains opening displacements (y-direction displacements in the local crack tip coordinate system).

As seen in the figure, the post-initiation displacement fields are dominated by the crack opening. With the exception of the 90° case (not shown), some sliding motion occurred in each test sample prior to crack initiation. In general, for each of the specimens tested, the opening mode displacements became more dominant in the post-initiation phase which is consistent with the extracted stress intensity factor histories (presented in later sections). The gray area in Fig. 14 is artificially widened for clarity. Due to the use of subset truncation, displacement data is available much closer to the physical crack.

Crack Tip Position from Automated Edge Detection Method

The crack tip positions were first extracted using the image processing-based edge detection method discussed earlier. From the crack tip position data, a quadratic Bezier function

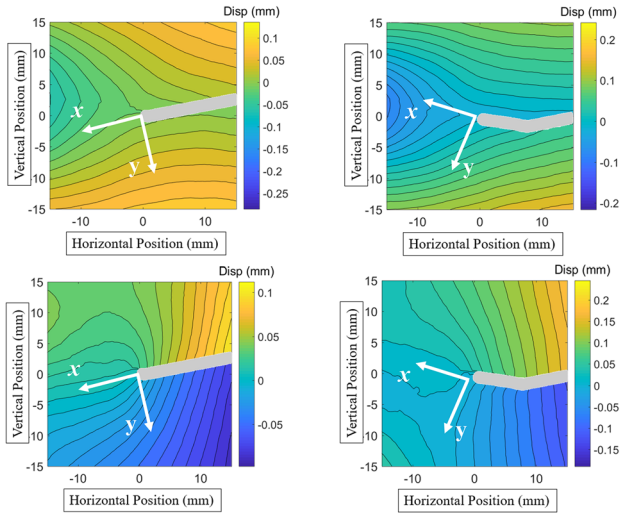

Fig. 14 Pre-initiation (left) and post-initiation (right) displacement contours from mixed mode experiment (80° initial crack inclination angle): Sliding mode (upper) and opening mode (lower); the width of the crack is artificially widened to better show the location of the tip

was used to evaluate crack tip velocity from the crack tip position estimations similar to what was used in [1]. For a given point, i, the smoothing function is evaluated as:

$$a_i(s) = (1-s)^2\hat{a}_i + 2s(1-s)\hat{a}_{i+1} + s^2\hat{a}_{i+2},\ 0 \le s \le 1 \quad (10)$$

where s is the smoothing parameter, $\hat{a}$ is the crack coordinate derived from the optical images, and a is the locally smoothed crack tip coordinate. A value of $s = 0.5$ was chosen for the present work which results in the middle point of the interval carrying the most weight in the smoothing function. The velocity is then evaluated using backward finite difference approximation as,

$$V_i = \frac{a_i - a_{i-1}}{t_i - t_{i-1}} \quad (11)$$

The crack tip positions and velocities for the 90°, 80°, and 65° experiments are plotted in Fig. 15.

The velocity histories for the three experiments generally reach a steady state crack propagation velocity between 250–300 m/s after a brief ramp up period. The experiments with 90° and 80° crack angles appear to have an initial period where the crack is accelerating whereas the 60° experiment appears to almost instantaneously reach the stable velocity. The velocities were all relatively consistent over the time window of 15 µs to 35 µs.

Crack Tip Position from Manual Identification

The crack tip positions were also extracted manually. The manual location of the crack tip was performed by selecting

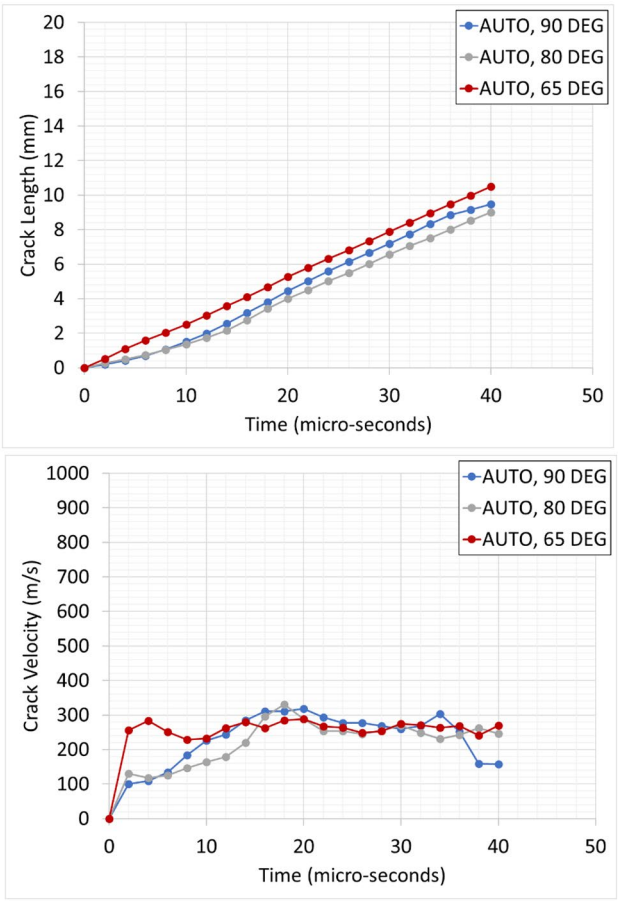

Fig. 15 Crack tip position histories (upper) extracted using automated Canny edge detection method and the corresponding velocity histories (lower)

the approximate location from a visual inspection of each speckle image. The selected location was separately viewed in the field of the displacement contours and the digital image correlation coefficients to determine its likelihood of being correct. This part of the process was particularly tedious and subjective to optical effects such as motion blur which make it difficult to follow the crack tip. The crack length and velocity histories are plotted in Fig. 16 for the 90°, 80°, and 65° cases. The displacement histories follow very similar monotonic trends in all cases.

A sharp rise in crack velocity was again evident in each case soon after crack initiation and the values attain a relatively constant value soon after the crack initiation transients have died out. Furthermore, the velocities seem rather consistent in the 250–350 m/s range for the three different crack inclination angles.

The automated and the manual crack tip detection methods resulted in similar crack velocity estimates. For instance, considering a temporal window between 15 and 40 µs the manual crack detection estimated a velocity of 312 m/s with

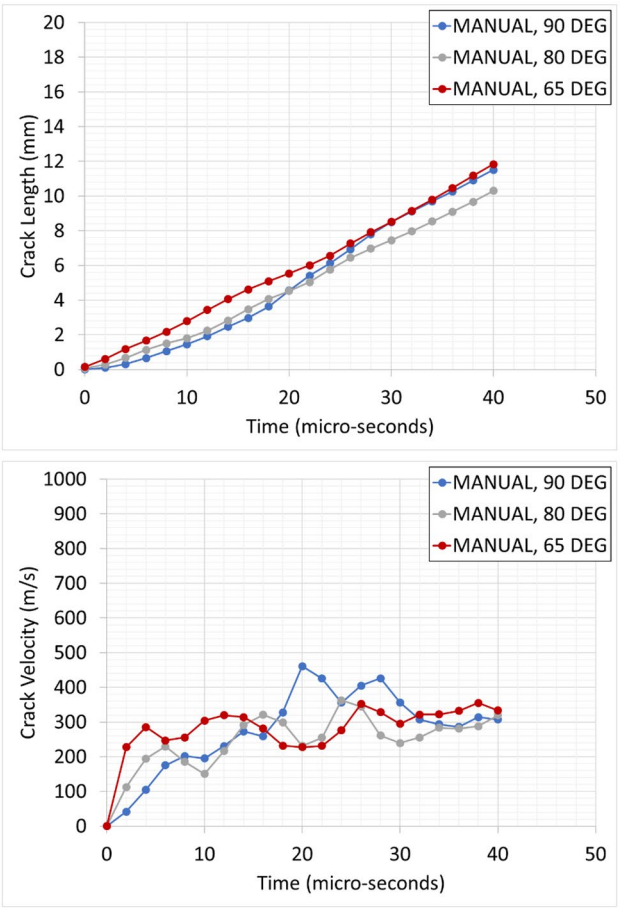

Fig. 16 Crack tip position histories (upper) extracted manually and the corresponding velocity histories (lower)

a standard deviation of 56 m/s whereas the edge detection algorithm estimated a propagation velocity of 265 m/s with a standard deviation of 34 m/s. This confirms that the two measurements are within 15% of each other across the majority of the propagation history. With the actual experimental displacement data, a set of crack tip location estimations were produced to determine the sensitivity of the method to variations in the thresholding criteria. The thresholding criteria is used to ensure that the point that is being tracked is above any noise level that may exist in locations within the field far away from the expected crack tip location. Recall that the current thresholding method first uses a histogram to estimate the noise in the field of partial derivative data far away from the crack faces. Using the noise estimate, a threshold value is calculated that is slightly above this noise estimate (e.g. 1.05X, 1.10X, etc.). Several threshold values were chosen to test the consistency of the output relative to the calculated threshold values. The crack tip position was very consistent regardless of threshold value provided that the threshold value was sufficiently above this lower noise estimate. This was reflected in the parametric study documented in earlier section and confirmed here. When implemented on the actual experimental data, across the 5 runs and the multiple crack tip position estimates obtained, the standard deviation was approximately 0.15 mm. This further illustrates that the edge detection algorithm is relatively insensitive to selection of this thresholding value. However, the value must be properly chosen based on the range of gradients present in the image and the amount of noise in the gradient field values away from the crack tip.

Stress Intensity Factor Histories

One of the key objectives of the edge detection technique is to show its fitness for automating the stress intensity factor extraction process. More specifically, the objective is to couple this technique to the hybrid DIC-FE method which has already been shown to be robust with respect to errors in crack tip position [30]. The stress intensity factors were extracted using four separate approaches tabulated in Table 5.

The processes for the second and fourth approaches are almost entirely automated with a minimal amount of intervention from the operator. The only noteworthy user intervention required is to initially trace out the crack path after the completion of the experiment. The various phases of the post-processing (as outlined in Fig. 1) occur in a series of MATLAB® scripts. Aside from the manual crack edge tracing, additional intervention is required to define additional necessary parameters (e.g. subset spacing, image scale factors, etc.) and start the execution of the various segments of the code. On the other hand, the first and fourth approaches require a significant amount of user intervention that requires, in many cases, a certain level of subjective interpretation of images for locating the crack tip.

Stress intensity factor histories are plotted in Fig. 17 for the three different mixed-mode dynamic experiments.

The first column of images shows the entire pre- and post-initiation mode I and mode II stress intensity factor histories for the three different experiments, with the post-initiation data being extracted using the automated crack tip identification method coupled with the hybrid DIC-FE results. Pre-initiation, the results of an elasto-dynamic finite element simulation are included for reference. Post-initiation crack growth is locally dominated by mode I conditions. During

Table 5 Stress intensity factor extraction methods

Group	Tracking Method	Extraction Method
1	Manual	Over-deterministic least-squares
2	Automated	Over-deterministic least-squares
3	Manual	DIC-FE
4	Automated	DIC-FE

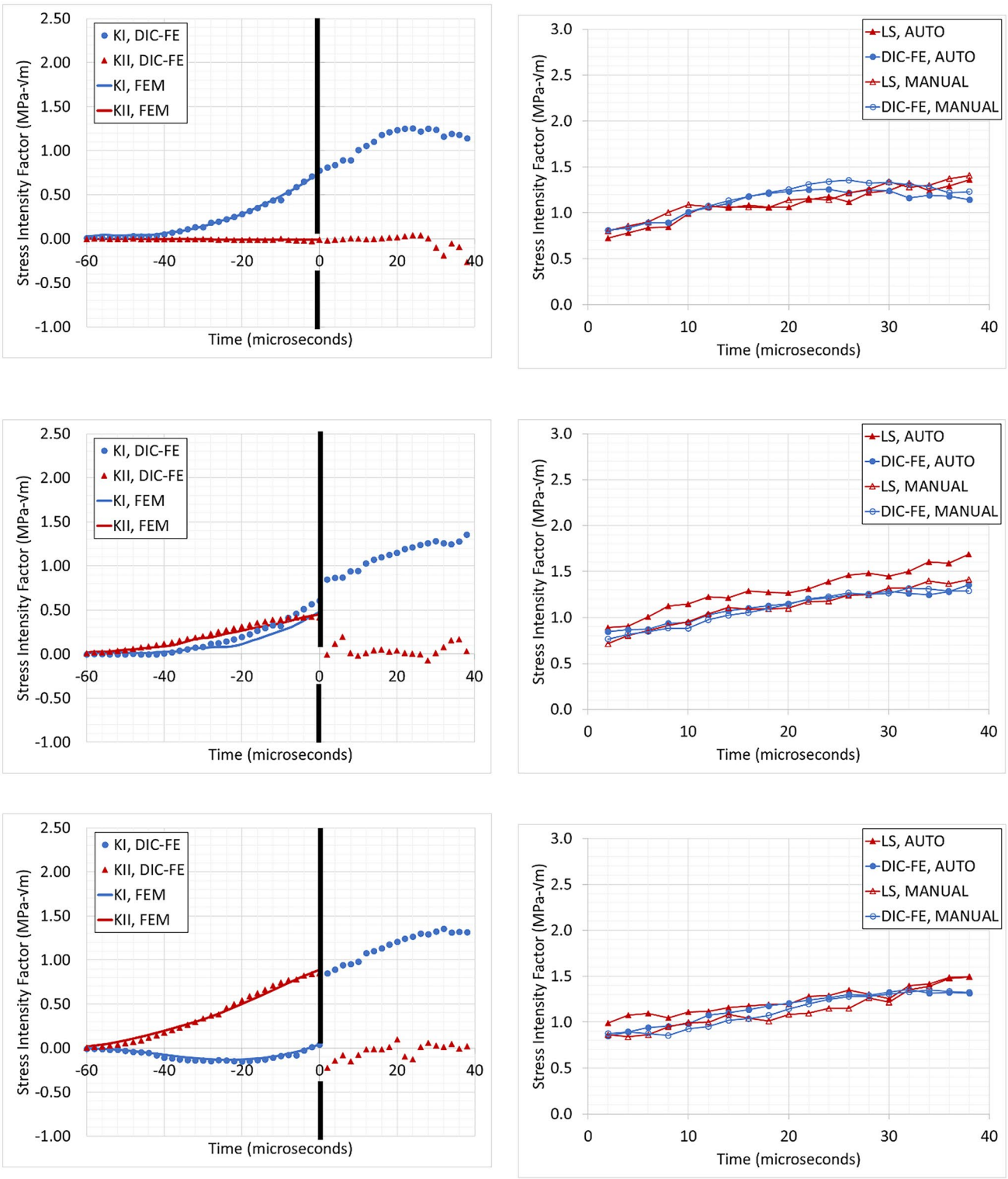

Fig. 17 Stress intensity factor histories for 90° (top), 80° (center), and 65° (bottom) dynamic experiments using different crack tip location methods. ($t = 0$ corresponds to crack initiation, right column is K_I only)

post processing, the crack tip coordinate system is aligned to the instantaneous local crack propagation direction, thus the mode II stress intensity factors in mixed-mode or mode II dominant cases drop to small values once the crack initiates (Note: $t = 0$ corresponds to crack initiation). The second column of plots show the post-initiation mode I stress intensity

Table 6 Average and standard deviation of post-initiation mode I stress intensity factors across the four methods

	K_I (MPa-$\sqrt{m}$)					
	Average			Standard Deviation		
Time (μs)	90°	80°	65°	90°	80°	65°
2	0.79	0.79	0.89	0.04	0.07	0.07
4	0.83	0.85	0.93	0.03	0.05	0.10
6	0.88	0.91	0.94	0.03	0.09	0.11
8	0.91	0.97	0.95	0.07	0.13	0.08
10	1.02	1.02	1.00	0.04	0.12	0.08
12	1.07	1.10	1.04	0.01	0.12	0.08
14	1.09	1.13	1.09	0.04	0.08	0.06
16	1.13	1.18	1.10	0.06	0.11	0.07
18	1.14	1.20	1.11	0.09	0.08	0.09
20	1.17	1.22	1.16	0.09	0.07	0.06
22	1.22	1.27	1.21	0.08	0.07	0.08
24	1.23	1.31	1.24	0.09	0.10	0.06
26	1.23	1.35	1.27	0.10	0.11	0.09
28	1.26	1.36	1.29	0.04	0.11	0.02
30	1.29	1.36	1.28	0.05	0.07	0.05
32	1.27	1.35	1.36	0.07	0.13	0.03
34	1.25	1.37	1.37	0.05	0.20	0.04
36	1.27	1.40	1.41	0.08	0.26	0.09
38	1.28	1.46	1.41	0.12	0.32	0.10

factor histories for each of the four methods listed in Table 5. The post-initiation mode II data are intentionally avoided for clarity since the values quickly trend toward 0.

It should be noted that the measurements were quite consistent across the four methods. The DIC-FE method (domain integral based) was particularly consistent between the manual and automated approaches. This is to be expected since it has been shown in prior works from the present authors [30] to be less sensitive to crack tip position. Conversely, the over-deterministic least-squares method had more variability as it is sensitive to several factors including crack tip position, crack orientation as well as the number of terms considered in the asymptotic expansion during analysis. To assess the variability across the four methods, the stress intensity values from each of the four methods was averaged and the standard deviation was evaluated. The calculations are summarized in Table 6. The summary shows that the typical standard deviation values were rather low relative to the average. This further illustrates the consistency as well as the utility of the automated method.

Conclusions

An automated, edge detection-based method has been introduced and critically evaluated for identifying crack tip positions for a dynamically propagating crack using optically measured displacement field data. The method utilizes a series a partial derivative computations from the displacement fields coupled with an adaptive thresholding approach to extract the locations of the crack faces and identify the crack tip. A series of verification tests were performed by generating displacement fields using numerical simulations on an edge-cracked geometry. The numerical simulations were used to investigate the selection of various parameters associated with the Canny-based edge detector. The parametric study helped identify the appropriate Gaussian filter parameters (5×5 kernel size with $\sigma \approx 1$), determine acceptable ranges of the thresholding parameter, and determine the relationship between subset spacing and error. The numerical simulations showed that the edge detection method could track the position of the crack tip accurately. Multiple dynamic fracture experiments were then performed to evaluate the instantaneous crack tip location and stress intensity factor histories for a propagating crack under mixed mode conditions.

Several key advancements relative to prior works are worth noting. First, the usage of subset truncation by decomposing the region of interest into multiple domains enables a more precise representation of displacement fields along each crack face and is a contributor to the success of the proposed approach. Also worthy of note is the usage of non-maximum suppression which is used in edge detection but has not necessarily been investigated

extensively for applying edge detection algorithms to fracture problems.

The results presented here are highly encouraging and suggest that the method is relatively robust for identifying the crack tip. Possibly the most important thing to note regarding the procedure is that it is repeatable and is able to estimate the crack tip positions in a matter of seconds due to its computational efficiency. For this analysis, a study of 10 images required approximately 9 s to pre-process and then approximately 0.5 s per image to locate the crack tip.

Appendix A

Non-maximum Suppression Procedure

A simple example with an edge running in the horizontal or vertical direction can be used to illustrate the concept of non-maximum suppression. A 5 × 5 excerpt from a random magnitude intensity field with an edge oriented in the vertical direction is shown in Fig. 18 with resulting simple gradient computations.

The gradient magnitude is calculated from the individual directional gradient values using equation (5) and the directions of the gradient vector can be computed using equation (6).

With the magnitude and direction of the partial derivatives known, the edge points can next be separated from the non-edge points. This information is used to adjudicate points within the field of gradient values that may be an actual edge, with the objective being to arrive at an edge that is exactly 1 data point wide. The first step here is to organize the partial derivative values according to direction, such that they are grouped into bins, [0°, 45°, 90°, 135°]. For the example problem illustrated here, the angles are tabulated in Fig. 19. For this example, since the values are primarily

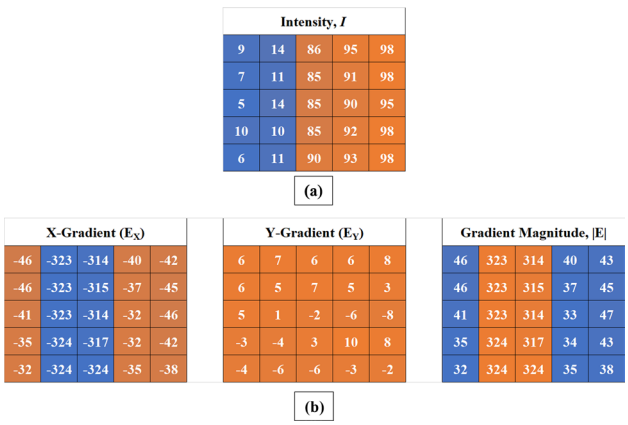

Fig. 18 Example intensity gradient a with edge running in vertical direction, and b example resulting gradient computation

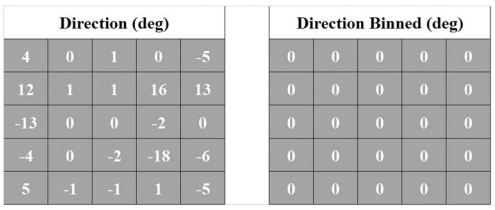

Fig. 19 Gradient direction calculations (left) and direction values binned to the nearest 45° increment (right)

dominated by the vertically oriented edge, all of the directions round to 0°.

With the directions known, each value can then be compared to the eight data points that surround it. More specifically, each point is compared to its neighboring points only in the direction of the angle of the gradient. For instance, if the direction is determined to be closest to the 45° direction, the data point is compared to the point to its upper right and lower left. The value at the given data point is then taken as the maximum of the 3 points along that direction. In the current example, the direction values are all 0°, thus each gradient value is only compared to its left or right neighbor as illustrated in Fig. 20.

Appendix B

Stress Intensity Factor Extraction Using Over-deterministic Least-squares Approach

For the displacement field around the crack tip prior to crack initiation, the over-deterministic least-squares results can be computed using the equations reported in [39] for the crack sliding (u_x) and crack opening displacements (u_y):

$$u_x = \sum_{n=1}^{N} \frac{(K_I)_n}{2\mu} \frac{r^{\frac{n}{2}}}{\sqrt{2\pi}} \left\{ \kappa \cos\frac{n}{2}\theta - \frac{n}{2}\cos\left(\frac{n}{2}-2\right)\theta + \left\{\frac{n}{2}-(-1)^n\right\}\cos\frac{n}{2}\theta \right\} + \sum_{n=1}^{N} \frac{(K_{II})_n}{2\mu} \frac{r^{\frac{n}{2}}}{\sqrt{2\pi}} \left\{ \kappa \sin\frac{n}{2}\theta - \frac{n}{2}\sin\left(\frac{n}{2}-2\right)\theta + \left\{\frac{n}{2}-(-1)^n\right\}\sin\frac{n}{2}\theta \right\} \tag{12}$$

Fig. 20 Original gradient values (left) with arrows showing the general direction along which maximum values are determined, resulting in the thinned matrix (right)

$$u_y = \sum_{n=1}^{N} \frac{(K_I)_n}{2\mu} \frac{r^{\frac{n}{2}}}{\sqrt{2\pi}} \left\{ \kappa \sin\frac{n}{2}\theta + \frac{n}{2}\sin\left(\frac{n}{2}-2\right)\theta - \left\{ \frac{n}{2} + (-1)^n \right\} \sin\frac{n}{2}\theta \right\} + \sum_{n=1}^{N} \frac{(K_{II})_n}{2\mu} \frac{r^{\frac{n}{2}}}{\sqrt{2\pi}} \left\{ -\kappa \cos\frac{n}{2}\theta - \frac{n}{2}\cos\left(\frac{n}{2}-2\right)\theta + \left\{ \frac{n}{2} - (-1)^n \right\} \cos\frac{n}{2}\theta \right\} \tag{13}$$

In the preceding equations, μ is the material shear modulus, and r and θ are the polar coordinates with crack tip as the origin and $\kappa = \frac{3-\upsilon}{1+\upsilon}$ for plane stress. The coefficients K_I and K_{II}, when $n = 1$, are the mode I and mode II stress intensity factors. For digital image correlation experiments, the u_x and u_y fields are known for a set of points in the polar coordinates r and θ.

By selecting a group of points in the vicinity of the crack, a set of equations can be formed to determine coefficients $(K_I)_n$ and $(K_{II})_n$. Using an over-deterministic approach, the experimental crack opening displacement can be used for extracting mode I fracture components whereas the crack sliding displacements can be used for mode II fracture components. However, it has been shown that by transforming experimentally measured in-plane Cartesian displacements into radial (u_r) and angular (u_θ) components, more accurate SIFs can be found in mixed mode problems [7]. That is, the Cartesian displacement components can be transformed into polar components as shown in equation (14).

$$\begin{Bmatrix} u_r \\ u_\theta \end{Bmatrix} = \begin{bmatrix} \cos\theta & \sin\theta \\ -\sin\theta & \cos\theta \end{bmatrix} \begin{Bmatrix} u_x \\ u_y \end{Bmatrix} \tag{14}$$

For the analyses presented in the present work, the radial (u_r) components are utilized for computing the SIFs. Using this technique, these equations can be expanded out to any number of higher order terms. For the present work, the equations were expanded for up to 10 terms and stress intensity factors were taken once K_I and K_{II} were determined to have converged. Measured displacement data was extracted for $0.5 \le {}^{r}/_{B} \le 1.5$ and $-120° \le \theta \le 120°$. The over-determined equation set was formed and solved for minimizing the least-squares error to compute values of K_I, K_{II} for the crack up to the point of initiation at a range of values of n.

Once the crack begins to propagate, the opening and sliding displacements can instead be written as:

$$u_x = \sum_{n=1}^{N} \frac{(K_I)_n B_I(C)}{2\mu} \sqrt{\frac{2}{\pi}}(n+1) \left\{ r_1^{n/2}\cos\frac{n}{2}\theta_1 - h(n) r_2^{n/2}\cos\frac{n}{2}\theta_2 \right\} + \sum_{n=1}^{N} \frac{(K_{II})_n B_{II}(C)}{2\mu} \sqrt{\frac{2}{\pi}}(n+1) \left\{ r_1^{n/2}\cos\frac{n}{2}\theta_1 - h(\bar{n}) r_2^{n/2}\cos\frac{n}{2}\theta_2 \right\} \tag{15}$$

$$u_y = \sum_{n=1}^{N} \frac{(K_I)_n B_I(C)}{2\mu} \sqrt{\frac{2}{\pi}}(n+1) \left\{ -\beta_1 r_1^{n/2}\sin\frac{n}{2}\theta_1 - \frac{h(n)}{\beta_2} r_2^{n/2}\sin\frac{n}{2}\theta_2 \right\} + \sum_{n=1}^{N} \frac{(K_{II})_n B_{II}(C)}{2\mu} \sqrt{\frac{2}{\pi}}(n+1) \left\{ \beta_1 r_1^{n/2}\cos\frac{n}{2}\theta_1 + \frac{h(\bar{n})}{\beta_2} r_2^{n/2}\cos\frac{n}{2}\theta_2 \right\} \tag{16}$$

In the above equations, μ is the material shear modulus, and r and θ are the polar coordinates with crack tip as the origin as before and $\kappa = \frac{3-\upsilon}{1+\upsilon}$ for plane stress. The longitudinal and shear wave speeds are defined as $C_L = \sqrt{\frac{(\kappa+1)\mu}{(\kappa-1)\rho}}$ and $C_S = \sqrt{\frac{\mu}{\rho}}$, respectively. The non-dimensional quantities, $\beta_1 = \sqrt{1 - \left(\frac{c}{C_L}\right)^2}$ and $\beta_2 = \sqrt{1 - \left(\frac{c}{C_S}\right)^2}$ are used to compute the spatial variations of $r_m = \sqrt{X^2 + \beta_m^2 Y^2}$ and $\theta_m = \tan^{-1}\left(\frac{\beta_m Y}{X}\right)$ based on the crack speed, c. Also, B_I, B_{II}, D, and h are defined in equation (17).

$$B_I(c) = \frac{\left(1+\beta_2^2\right)}{D},\ B_{II}(c) = \frac{2\beta_2}{D}$$
$$D = 4\beta_1\beta_2 - \left(1+\beta_2^2\right)^2$$
$$h(n) = \begin{cases} \frac{2\beta_1\beta_2}{1+\beta_2^2} & \text{for even } n \\ \frac{1+\beta_2^2}{2} & \text{for odd } n \end{cases}$$
$$h(\bar{n}) = h(n+1) \tag{17}$$

Appendix C

Mapping from FE-space to Uniformly Gridded Space

As previously stated, the FE model is comprised of a variety of element shapes due to geometry around the crack, and therefore, does not create output on a uniformly spaced grid of points. A mapping procedure is thus necessary to create a uniformly spaced grid of displacement data for testing the algorithm. To that end, an inverse FE mapping technique was created to generate displacement fields. In the mapper developed for the current effort, the input file for the source finite element model contains all of the node numbers, nodal coordinates, and element connectivity. For each of the 4-noded elements in the finite element model, the mapper locates the grid points that reside within its boundaries using a polygon search algorithm coded in MATLAB®. Since the element shape could be in the form of any four-sided polygon, potentially distorted, a numerical routine was then used to determine the parametric coordinates of each of the destination grid points within the space of their parent source

element in the original model. An example of the dissimilarity between the two data point locations is shown in Fig. 21. A set of x- and y-coordinates on a uniform grid was created at the desired "output" point locations, as shown in red. The source model elements and nodes are shown in black. The relationship between the global space and the parametric space is also illustrated in Fig. 21 with an example map-to point shown by the dark-shaded point, x_p.

The global coordinate of any point within the boundary of the element is a function of the parametric equation, N, and the global coordinates of the nodes that define the boundary of the polygon. For a 4-noded quadrilateral element, the global coordinate of a point, x_p and y_p,, is defined in equation (18).

$$(x_p;y_p) = \sum_{i=1}^{4} N_i(\xi,\eta)(x_i;y_i) \tag{18}$$

where i is the node number, x_i and y_i are the global coordinates of the i-th node and ξ and η are the parametric coordinates.

The parametric equations, N, for a quadrilateral element are [40]:

$$\begin{aligned} N_1 &= \tfrac{1}{4}(1-\xi)(1-\eta) \\ N_2 &= \tfrac{1}{4}(1+\xi)(1-\eta) \\ N_3 &= \tfrac{1}{4}(1+\xi)(1+\eta) \\ N_4 &= \tfrac{1}{4}(1-\xi)(1+\eta) \end{aligned} \tag{19}$$

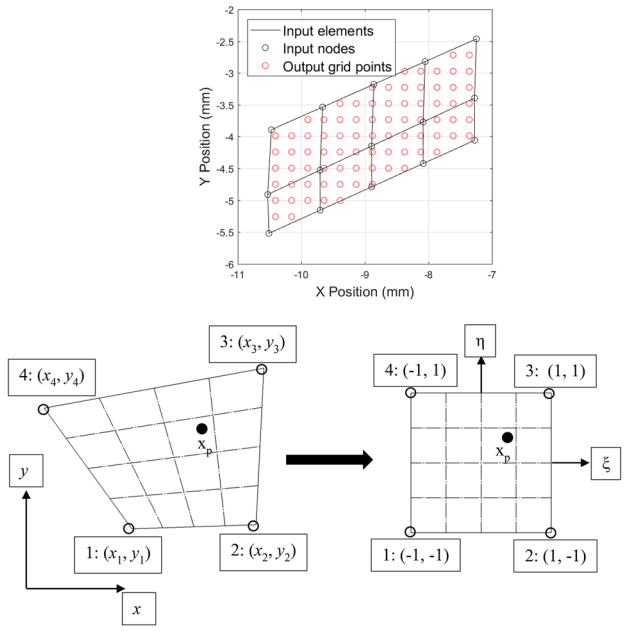

Fig. 21 Example to show dissimilarity between simulated data and gridded data near crack faces (top) and mapping from global coordinate space to parametric coordinate space (bottom)

The parametric coordinates, ξ and η, for the target output point can be located using an iterative procedure. For a given iteration, the parametric space is split up into a 5 × 5 grid of points. The values of ξ and η, are used to calculate the resulting global coordinates at each of these points on the 5 × 5 grid. The point within the grid that results in coordinates that have the shortest Euclidean distance to the actual point of interest is used as the initial guess of the next iteration. That initial guess becomes the center point of a smaller 5 × 5 grid that is part of a subdivision of the grid in the previous iteration. This iterative process continues to subdivide the parametric space into smaller and smaller 5 × 5 grids until a result is found that matches the coordinates of the desired point within an acceptable tolerance. For the present work, the algorithm was required to determine the values of ξ and η that resulted in an error between the calculated coordinates and the actual coordinates of less than 1e-6. While there are more efficient numerical techniques for this part of the process, this approach converges reasonably quickly, usually within 6–8 iterations and is relatively inexpensive computationally. The approach can suffer some difficulty when the elements are significantly distorted. However, for the present work, the mesh was controlled sufficiently upfront and significant element distortions were avoided.

For a given point of interest in the grid that is being mapped to, once the parametric coordinates are known with an acceptable accuracy, any desirable field quantities can then be calculated. For this work, the field quantities of interest namely, displacements in the vertical and horizontal directions, the following relationships are used to compute those values:

$$(u_p;v_p) = \sum_{i=1}^{4} N_i(\xi,\eta)(u_i;v_i). \tag{20}$$

This method is particularly advantageous because it avoids issues with averaging or smoothing around the crack tip or across the crack faces in the source data. This is because the target grid points are associated with elements from the output data. The nodal connectivity for the source elements is inherited from the source finite element model. Since the original mesh is created without elements spanning the crack tip or bridging across the crack faces, no averaging occurs due to target nodes on one side of the crack face being influenced by displacements of nodes on the opposing side of the crack. It should be noted that in the case of a set of points that are arranged in a rectangular fashion, this general method simplifies to bilinear interpolation.

Acknowledgements Partial support for this work under US Army Research Office grant W911NF-22-1-0015 is gratefully acknowledged.

Declarations

Conflicts of Interest The authors declare that they have no known competing financial interests or personal relationships that could have ap-

peared to influence the work reported in this paper. Dr. Hareesh Tippur currently serves as the Chair of the International Advisory Board of Experimental Mechanics.

References

1. Lee D, Tippur HV, Bogert P (2009) Experimental study of dynamic crack growth in unidirectional graphite/epoxy composites using digital image correlation method and high-speed photography. J Compos Mater 43(19):2081–2108
2. Sundaram BM, Tippur HV (2018) Full-field measurement of contact-point and crack-tip. Int J Appl Glas Sci 9:123–136
3. Dondetti S, Tippur HV (2019) A comparative study of dynamic fracture of soda-lime glass using photoelasticity, digital image correlation and digital gradient sensing techniques. Exp Mech 60:217–233
4. Redner AS (1977) Experimental determination of stress intensity factors: A review of photoelastic approaches. International Conference on Fracture Mechanics and Technology, Hong Kong
5. Etheridge JM, Dally JW (1977) A critical review of methods for determining stress-intensity factors from isochromatic patterns. Exp Mech 17(7):248–254
6. McNeil SR, Peters WH, Sutton MA (1987) Estimation of stress intensity factor by digital image correlation. Eng Fract Mech 28:101–112
7. Yoneyama S, Takashi M (2001) Automatic determination of stress intensity factor utilizing digitial image correlation. J Jpn Soc Exp Mech 1:202–206
8. Sanford RJ (1980) Application of the least-squares method to photoelastic analysis. Exp Mech 20:192–197
9. Pacey MN, James MN, Patterson EA (2005) A new photoelastic model for studying fatigue crack closure. Exp Mech 45(1):42–52
10. Roux S, Hild F (2006) Stress intensity factor measurements from digital image correlation: post-processing and integrated approaches. Int J Fract 140:141–157
11. Hamam R, Hild F, Roux S (2007) Stress intensity factor gauging by digital image correlation: Application in cyclic fatigue. Strain 43:181–192
12. Zanganeh M, Lopez-Crespo P, Tai YH, Yates JR (2013) Locating the crack tip using displacement field data: A comparative study. Strain 49:102–115
13. Rethore J (2015) Automatic crack tip detection and stress intensity factor estimation of curved cracks from digital images. Int J Numer Meth Eng 103:516–534
14. Abdel-Qader I, Abdudayyeh O, Kelly ME (2003) Analysis of edge-detection techniques for crack identification in bridges. J Comput Civ Eng 17(4):255–263
15. Lopez-Crespo P, Shterenlikht A, Patterson EA, Yates JR, Withers PJ (2008) The stress intensity of mixed mode cracks determined by digital image correlation. J Strain Anal 43:769–780
16. Lopez-Crespo P, Burguete RL, Patterson EA, Shterenlikht A, Withers PJ, Yates JR (2009) Study of a crack at a fastener hole by digital image correlation. Exp Mech 49:551–559
17. Strohmann T, Starostin-Penner D, Breitbarth E, Requena G (2021) Automatic detection of fatigue crack paths using digital image correlation and convolutional neural networks. Fatigue Fract Eng Mater Struct 44:1336–1348
18. Miao S, Pan P, Li S, Chen J, Konicek P (2021) Quantitative fracture analysis of hard rock containing double infilling flaws with a novel DIC-based method. Eng Fract Mech 252:107846
19. Peters W, Ranson W (1982) Digital Imaging Techniques in Experimental Stress Analysis. Opt Eng 21(3):427–432
20. Sutton MA, Wolters WJ, Peters WJ, Peters WH, Ranson WF, McNeill SR (1983) Determination of displacements using an improved digital correlation method. Image Vis Comput 1(3):133–139
21. Peters WH, Ranson WF, Sutton MA, Chu T, Anderson J (1983) Applications of Digital Correlation Methods to Rigid Body Mechanics. Opt Eng 22(6):738–742
22. Chu TC, Ranson MA, Sutton MA (1985) Applications of digital-image-correlation techniques to experimental mechanics. Exp Mech 25(3):232–244
23. Schreier H, Orteu J-J, Sutton MA (2009) Image Correlation for Shape, Motion and Deformation Measurements. Springer, New York, NY
24. Canny J (1986) A computational approach to edge detection. IEEE Trans Pattern Anal Mach Intell 8(6):679–698
25. McIlhagga W (2011) The Canny edge detector revisited. Int J Comput Vision 91:251–261
26. Sobel I, Feldman G (1968) A 3X3 isotropic gradient operator for image processing. Stanford Artificial Intelligence Project
27. Rong W, Li Z, Zhang W, Sun L (2014) An improved Canny edge detection algorithm. 2014 IEEE international conference on mechatronics and automation. IEEE, pp 577–582
28. Shih CF, Moran B, Nakamura T (1986) Energy release rate along a three-dimensional crack front in a thermally stressed body. Int J Fract 30:79–102
29. Shih CF, Asaro R (1988) Elastic-plastic analysis of cracks on bimaterial interfaces: Part I: Small scale yielding. J Appl Mech 55(2):299–316
30. Owens AT, Tippur HV (2021) Measurement of mixed-mode fracture characteristics of an epoxy-based adhesive using a hybrid Digital Image Correlation (DIC) and Finite Elements (FE) approach. Opt Lasers Eng 140:106544
31. Isaac JP, Dondeti S, Tippur HV (2020) Crack initiation and growth in additively printed ABS: Effect of print architecture studied using DIC. Addit Manuf 36:101536
32. Chong KP, Kuruppu MD (1984) New specimen for fracture toughness determination for rock and other materials. Int J Fract 26:R49–R62
33. Chong KP, Kuruppu MD, Kuszmaul JS (1987) Fracture toughness determination of rocks with core-based specimens. SEM/RILEM International Conference on Fracture of Concrete and Rocks, Texas
34. Lim IL, Johnston IW, Choi SK (1993) Stress intensity factors for semi-circular specimens under three-point bending. Eng Fract Mech 44(3):363–382
35. Samareh J (2007) Discrete data transfer technique for fluid-structure interaction. 18th AIAA Computational Fluid Dynamics Conference
36. Silva GHC, Le Riche R, Molimard J, Vautrin A (2009) Exact and efficient interpolation using finite elements shape functions. Eur J Comput Mech 18(3–4):307–331
37. Blaber J, Adair B, Antoniou A (2015) Ncorr: Open-source 2D digital image correlation Matlab software. Exp Mech 55(6):1105–1122
38. Owens AT, Tippur HV (2022) Mixed-mode dynamic fracture behavior of an epoxy adhesive under stress wave loading. Eng Fract Mech 276, Part A, 108833
39. Westergaard HM (1939) Bearing pressure and cracks. J Appl Mech 6:49–53
40. Hua C (1990) An inverse transformation for quadrilateral isoparametric elements: Analysis and application. Finite Elem Anal Des 7:159–166